Physical limitations on broadband scattering by heterogeneous obstacles

Sohl, Christian; Gustafsson, Mats; Kristensson, Gerhard

2006

CODEN:LUTEDX/(TEAT-7151)/1-25/(2006)

Physical limitations on broadband scattering by heterogeneous obstacles

Christian Sohl, Mats Gustafsson, and Gerhard Kristensson

Electromagnetic Theory
Department of Electroscience
Lund University
Sweden

Christian Sohl, Mats Gustafsson, and Gerhard Kristensson

Department of Electroscience
Electromagnetic Theory
P.O. Box 118
SE-221 00 Lund
Sweden

Editor: Gerhard Kristensson

Abstract

In this paper, new physical limitations on the extinction cross section and broadband scattering are investigated. A measure of broadband scattering in terms of the integrated extinction is derived for a large class of scatterers based on the holomorphic properties of the forward scattering dyadic. Closed-form expressions of the integrated extinction are given for the homogeneous ellipsoids, and theoretical bounds are discussed for arbitrary heterogeneous scatterers. Finally, the theoretical results are illustrated by numerical computations for a series of generic scatterers.

1 Introduction

The relation between the extinction cross section and the forward scattering dyadic, nowadays known as the optical theorem, dates back to the work of Rayleigh more than a century ago [26]. Since then, the concept has fruitfully been extended to high-energy physics where it today plays an essential role in analyzing particle collisions [20]. This is one striking example of how results, with minor modifications, can be used in both electromagnetic and quantum mechanic scattering theory. Another example of such an analogy is presented in this paper, and it is believed that more analogies of this kind exist, see *e.g.*, the excellent books by Taylor [27] and Nussenzveig [22].

As far as the authors know, a broadband measure for scattering of electromagnetic waves was first introduced by Purcell [24] in 1969 concerning absorption and emission of radiation by interstellar dust. Purcell derived the integrated extinction for a very narrow class of scatterers via the Kramers-Kronig relations [17, pp. 279–283]. A slightly different derivation of the same result was done by Bohren and Huffman [4, pp. 116–117]. In both references it was noticed that the integrated extinction is proportional to the volume of the scatterer, with proportionality factor depending only on the shape and the long wavelength limit response of the scatterer. Based upon this observation, Bohren and Huffman conjecture [4, p. 117]:

> *Regardless of the shape of the particle, however, it is plausible on physical grounds that integrated extinction should be proportional to the volume of an arbitrary particle, where the proportionality factor depends on its shape and static dielectric function.*

Curiosity whether this supposition is true and the generalization of the results to a wider class of scatterers have been the main driving forces of the present study.

Physical limitations on scattering of electromagnetic waves play an important role in the understanding of wave interaction with matter. Specifically, numerous papers addressing physical limitations in antenna theory are found in the literature. Unfortunately, they are almost all restricted to the spherical geometry, deviating only slightly from the pioneering work of Chu [5] in 1948. In contrast to antenna theory, there are, however, few papers addressing physical limitations in scattering by electromagnetic waves. An invaluable exception is given by the fundamental work

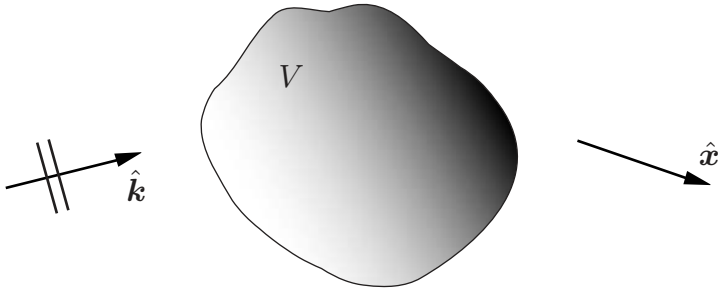

Figure 1: Illustration of the scattering problem. The scatterer V is subject to a plane wave incident in the $\hat{\boldsymbol{k}}$-direction.

of Nussenzveig [21] in which both scattering by waves and particles are analyzed in terms of causality. Other exceptions of importance for the present paper are the Rayleigh scattering bounds derived by Jones [10, 11].

The results of Purcell mentioned above are generalized in several ways in this paper. The integrated extinction is proved to be valid for anisotropic heterogeneous scatterers of arbitrary shape. Specifically, this quantity is analyzed in detail for the ellipsoidal geometry. Several kinds of upper and lower bounds on broadband scattering for isotropic material models are presented. These limitations give a means of determining if an extinction cross section is obtainable or not.

The paper is organized as follows: in Section 2, the integrated extinction is derived for a large class of scatterers based on the holomorphic properties of the forward scattering dyadic. Next, in Section 3, bounds on broadband scattering are discussed for arbitrary isotropic heterogeneous scatterers. In the following section, Section 4, some closed-form expressions of the integrated extinction are given. Moreover, in Section 5, numerical results on the extinction cross section are presented and compared with the theoretical bounds. Finally, some future work and possible applications are discussed in Section 6.

Throughout this paper, vectors are denoted in italic bold face, and dyadics in roman bold face. A hat (ˆ) on a vector denotes that the vector is of unit length.

2 Broadband scattering

The scattering problem considered in this paper is Fourier-synthesized plane wave scattering by a bounded heterogeneous obstacle of arbitrary shape, see Figure 1. The scatterer is modeled by the anisotropic constitutive relations [17, Ch. XI] and assumed to be surrounded by free space. The analysis presented in this paper includes the perfectly conducting material model, as well as general dispersion with or without a conductivity term.

2.1 The forward scattering dyadic

The scattering properties of V are described by the far field amplitude, $\boldsymbol{F}$, defined in terms of the scattered field, $\boldsymbol{E}_\mathrm{s}$, as [15, Sec. 2]

$$\boldsymbol{E}_\mathrm{s}(t, \boldsymbol{x}) = \frac{\boldsymbol{F}(\mathrm{c}_0 t - x\hat{\boldsymbol{x}})}{x} + \mathcal{O}(x^{-2}) \quad \text{as } x \to \infty, \tag{2.1}$$

where c_0 is the speed of light in vacuum, and $\hat{\boldsymbol{x}} = \boldsymbol{x}/x$ with $x = |\boldsymbol{x}|$. The far field amplitude is related to the incident field, $\boldsymbol{E}_\mathrm{i}(\mathrm{c}_0 t - \hat{\boldsymbol{k}} \cdot \boldsymbol{x})$, which is impinging in the $\hat{\boldsymbol{k}}$-direction, via the linear and time-translational invariant convolution

$$\boldsymbol{F}(\tau, \hat{\boldsymbol{x}}) = \int_{-\infty}^{\infty} \mathbf{S}_\mathrm{t}(\tau - \tau', \hat{\boldsymbol{k}}, \hat{\boldsymbol{x}}) \cdot \boldsymbol{E}_\mathrm{i}(\tau') \, \mathrm{d}\tau'.$$

The dimensionless temporal scattering dyadic $\mathbf{S}_\mathrm{t}$ is assumed to be causal in the forward direction, $\hat{\boldsymbol{k}}$, in the sense that the scattered field cannot precede the incident field [21, pp. 15–16], *i.e.*,

$$\mathbf{S}_\mathrm{t}(\tau, \hat{\boldsymbol{k}}, \hat{\boldsymbol{k}}) = 0 \quad \text{for } \tau < 0. \tag{2.2}$$

The Fourier transform of (2.1) evaluated in the forward direction is

$$\boldsymbol{E}_\mathrm{s}(k, x\hat{\boldsymbol{k}}) = \frac{\mathrm{e}^{\mathrm{i}kx}}{x} \mathbf{S}(k, \hat{\boldsymbol{k}}) \cdot \boldsymbol{E}_0 + \mathcal{O}(x^{-2}) \quad \text{as } x \to \infty,$$

where k is a complex variable in the upper half plane with $\operatorname{Re} k = \omega/\mathrm{c}_0$. Here, the amplitude of the incident field is $\boldsymbol{E}_0$, and the forward scattering dyadic, $\mathbf{S}$, is given by the Fourier representation

$$\mathbf{S}(k, \hat{\boldsymbol{k}}) = \int_{0^-}^{\infty} \mathbf{S}_\mathrm{t}(\tau, \hat{\boldsymbol{k}}, \hat{\boldsymbol{k}}) \mathrm{e}^{\mathrm{i}k\tau} \, \mathrm{d}\tau. \tag{2.3}$$

The imaginary part of k improves the convergence of (2.3) and extends the elements of $\mathbf{S}$ to holomorphic functions in the upper half plane for a large class of dyadics $\mathbf{S}_\mathrm{t}$. Recall that $\mathbf{S}(\mathrm{i}k, \hat{\boldsymbol{k}})$ is real-valued for real-valued k and $\mathbf{S}(\mathrm{i}k, \hat{\boldsymbol{k}}) = \mathbf{S}^*(-\mathrm{i}k^*, \hat{\boldsymbol{k}})$ [21, Sec. 1.3–1.4].

The scattering cross section σ_s and absorption cross section σ_a are defined as the ratio of the scattered and absorbed power, respectively, to the incident power flow density in the forward direction. The sum of the scattering and absorption cross sections is the extinction cross section,

$$\sigma_\mathrm{ext} = \sigma_\mathrm{s} + \sigma_\mathrm{a}.$$

The three cross sections are by definition real-valued and non-negative. The extinction cross section is related to the forward scattering dyadic, $\mathbf{S}$, via the optical theorem [20, pp. 18–20]

$$\sigma_\mathrm{ext}(k) = \frac{4\pi}{k} \operatorname{Im} \left\{ \hat{\boldsymbol{p}}_\mathrm{e}^* \cdot \mathbf{S}(k, \hat{\boldsymbol{k}}) \cdot \hat{\boldsymbol{p}}_\mathrm{e} \right\}. \tag{2.4}$$

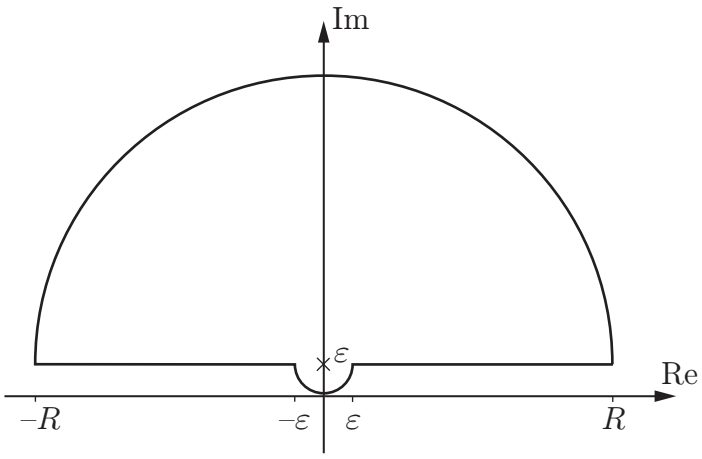

Figure 2: Integration contour used in the Cauchy integral theorem in (2.5).

Here, k is real-valued, and $\hat{\boldsymbol{p}}_{\mathrm{e}} = \boldsymbol{E}_0/|\boldsymbol{E}_0|$ is a complex-valued vector, independent of k, that represents the electric polarization, and, moreover, satisfies $\hat{\boldsymbol{p}}_{\mathrm{e}} \cdot \hat{\boldsymbol{k}} = 0$.

The holomorphic properties of $\mathbf{S}$ can be used to determine an integral identity for the extinction cross section. To simplify the notation, let $\rho(k) = \hat{\boldsymbol{p}}_{\mathrm{e}}^* \cdot \mathbf{S}(k, \hat{\boldsymbol{k}}) \cdot \hat{\boldsymbol{p}}_{\mathrm{e}}/k^2$. The Cauchy integral theorem with respect to the contour in Figure 2 then yields

$$\rho(\mathrm{i}\varepsilon) = \int_0^\pi \frac{\rho(\mathrm{i}\varepsilon - \varepsilon \mathrm{e}^{\mathrm{i}\phi})}{2\pi}\, \mathrm{d}\phi + \int_0^\pi \frac{\rho(\mathrm{i}\varepsilon + R\mathrm{e}^{\mathrm{i}\phi})}{2\pi}\, \mathrm{d}\phi + \int_{\varepsilon<|k|<R} \frac{\rho(k+\mathrm{i}\varepsilon)}{2\pi \mathrm{i} k}\, \mathrm{d}k, \quad (2.5)$$

where k in the last integral on the right hand side is real-valued.

The left hand side of (2.5) and the integrand in the first integral on the right hand side are well-defined in the limit $\varepsilon \to 0$ and given by the long wavelength limit [15, p. 18]

$$\rho(\varepsilon) = \frac{1}{4\pi} (\hat{\boldsymbol{p}}_{\mathrm{e}}^* \cdot \boldsymbol{\gamma}_{\mathrm{e}} \cdot \hat{\boldsymbol{p}}_{\mathrm{e}} + \hat{\boldsymbol{p}}_{\mathrm{m}}^* \cdot \boldsymbol{\gamma}_{\mathrm{m}} \cdot \hat{\boldsymbol{p}}_{\mathrm{m}}) + \mathcal{O}(\varepsilon) \quad \text{as } \varepsilon \to 0. \quad (2.6)$$

Here, $\hat{\boldsymbol{p}}_{\mathrm{m}} = \hat{\boldsymbol{k}} \times \hat{\boldsymbol{p}}_{\mathrm{e}}$ denotes the magnetic polarization and $\boldsymbol{\gamma}_{\mathrm{e}}$ and $\boldsymbol{\gamma}_{\mathrm{m}}$ are the electric and magnetic polarizability dyadics, respectively, see Appendix A for their explicit definitions. These dyadics are real-valued and symmetric. This result also includes the effect of a conductivity term [15, pp. 49–51].

The second term on the right hand side of (2.5) is assumed to approach zero and does not contribute in the limit $R \to \infty$. This is physically reasonable since the short wavelength response of a material is non-unique from a modeling point of view [8]. For a large class of scatterers the integrand is also proportional to the projected area, A, in the forward direction according to the extinction paradox [29, pp. 107–113], *i.e.*,

$$\rho(k) = -\frac{A(\hat{\boldsymbol{k}})}{2\pi \mathrm{i} k} \left(1 + \mathcal{O}(|k|^{-1})\right) \quad \text{as } |k| \to \infty, \qquad \operatorname{Im} k \geq 0.$$

The constant A is real-valued since $\mathbf{S}(\mathrm{i}k, \hat{\boldsymbol{k}})$ is real-valued for real-valued k.

In the last term on the right hand side of (2.5) it is assumed that ρ is sufficiently regular to extend the contour to the real axis. Under this assumption, the real part of (2.5) yields

$$\operatorname{Re}\rho(0) = \frac{1}{\pi}\int_{-\infty}^{\infty} \frac{\operatorname{Im}\rho(k)}{k}\ \mathrm{d}k = \frac{1}{4\pi^2}\int_{-\infty}^{\infty} \frac{\sigma_{\mathrm{ext}}(k)}{k^2}\ \mathrm{d}k = \frac{1}{4\pi^3}\int_0^{\infty} \sigma_{\mathrm{ext}}(\lambda)\,\mathrm{d}\lambda, \quad (2.7)$$

where we have used the optical theorem, (2.4). In this expression $\lambda = 2\pi/k$ is the vacuum wavelength.

In fact, the assumptions on ρ can be relaxed, and the analysis can be generalized to certain classes of distributions [21, pp. 33–43]. However, the integral in (2.7) is classically well-defined for the examples considered in this paper. The relation (2.7) can also be derived using the Hilbert transform [28, Ch. V].

2.2 The integrated extinction

We are now ready to utilize the main result in the previous section. Moreover, the properties of the polarizability dyadics are exploited, and the important results of Jones are invoked.

Insertion of the long wavelength limit (2.6) into (2.7) yields the integrated extinction

$$\int_0^{\infty} \sigma_{\mathrm{ext}}(\lambda)\ \mathrm{d}\lambda = \pi^2\left(\hat{\boldsymbol{p}}_{\mathrm{e}}^{*}\cdot\boldsymbol{\gamma}_{\mathrm{e}}\cdot\hat{\boldsymbol{p}}_{\mathrm{e}} + \hat{\boldsymbol{p}}_{\mathrm{m}}^{*}\cdot\boldsymbol{\gamma}_{\mathrm{m}}\cdot\hat{\boldsymbol{p}}_{\mathrm{m}}\right). \quad (2.8)$$

Note that (2.8) is independent of dispersion, depending only on the long wavelength limit response of the scatterer in terms of $\boldsymbol{\gamma}_{\mathrm{e}}$ and $\boldsymbol{\gamma}_{\mathrm{m}}$. Closed-form expressions of $\boldsymbol{\gamma}_{\mathrm{e}}$ and $\boldsymbol{\gamma}_{\mathrm{m}}$ exist for the homogeneous ellipsoids, see Section 4. The polarizability dyadics for more general obstacles are summarized in Kleinman & Senior [15, p. 31].

For pure electric ($\boldsymbol{\gamma}_{\mathrm{m}} = \mathbf{0}$) and pure magnetic ($\boldsymbol{\gamma}_{\mathrm{e}} = \mathbf{0}$) scatterers, the integrated extinction depends only on $\hat{\boldsymbol{p}}_{\mathrm{e}}$ and $\hat{\boldsymbol{p}}_{\mathrm{m}}$, respectively, and hence not on $\hat{\boldsymbol{k}} = \hat{\boldsymbol{p}}_{\mathrm{e}} \times \hat{\boldsymbol{p}}_{\mathrm{m}}$. Moreover, the integrated extinction for a scatterer with isotropic polarizability dyadics, *i.e.*, $\boldsymbol{\gamma}_{\mathrm{e}} = \gamma_{\mathrm{e}}\mathbf{I}$ and $\boldsymbol{\gamma}_{\mathrm{m}} = \gamma_{\mathrm{m}}\mathbf{I}$, is independent of $\hat{\boldsymbol{p}}_{\mathrm{e}}$ and $\hat{\boldsymbol{p}}_{\mathrm{m}}$ as well as $\hat{\boldsymbol{k}}$.

An important variational result can be established for isotropic material parameters with the long wavelength limit response given by the electric and magnetic susceptibilities, $\chi_{\mathrm{e}}(\boldsymbol{x})$ and $\chi_{\mathrm{m}}(\boldsymbol{x})$, respectively. The result states that the integrated extinction increase monotonically with increasing $\chi_{\mathrm{e}}(\boldsymbol{x})$ and $\chi_{\mathrm{m}}(\boldsymbol{x})$ for each $\boldsymbol{x} \in \mathbb{R}^3$ [11, Thm. 1], *i.e.*,

$$\chi_{i1}(\boldsymbol{x}) \le \chi_{i2}(\boldsymbol{x}), \quad \boldsymbol{x} \in \mathbb{R}^3 \quad \Longrightarrow \quad \int_0^{\infty} \sigma_{\mathrm{ext}1}(\lambda)\ \mathrm{d}\lambda \le \int_0^{\infty} \sigma_{\mathrm{ext}2}(\lambda)\ \mathrm{d}\lambda, \quad (2.9)$$

where $i = \mathrm{e}, \mathrm{m}$. Recall that Kramers-Kronig relations [17, pp. 279–281] implies that $\chi_{\mathrm{e}}(\boldsymbol{x})$ and $\chi_{\mathrm{m}}(\boldsymbol{x})$ pointwise are non-negative, provided the conductivity is zero. If the conductivity of the scatterer is non-zero, the electric polarizability dyadic, $\boldsymbol{\gamma}_{\mathrm{e}}$, can be determined by letting the electric susceptibility becoming infinitely large [15, pp. 49–50]. As a consequence of (2.9), no heterogeneous scatterer has a larger integrated extinction than the corresponding homogeneous one with maximal susceptibility.

An important model in many applications is the perfectly conducting case (PEC), which is formally obtained — in the long wavelength limit — by the limits [15, pp. 39–40]

$$\chi_{\mathrm{e}}(\boldsymbol{x}) \to \infty \quad \text{and} \quad \chi_{\mathrm{m}}(\boldsymbol{x}) \searrow -1. \tag{2.10}$$

Since the long wavelength limit lacks a natural length scale it follows that the integrated extinction for any heterogeneous scatterer is proportional to the volume $|V| = \int_V \mathrm{dV}_{\boldsymbol{x}}$, where $\mathrm{dV}_{\boldsymbol{x}}$ is the volume measure with respect to $\boldsymbol{x}$ — a result conjectured by Bohren and Huffman [4, p. 117] for spherical scatterers. A brief derivation of this statement for inhomogeneous, anisotropic material parameters is presented in Appendix A.

Randomly oriented scatterers are valuable in many applications [24]. The broadband scattering properties of an ensemble of randomly oriented scatterers is quantified by the averaged integrated extinction,

$$\int_0^\infty \bar{\sigma}_{\mathrm{ext}}(\lambda)\ \mathrm{d}\lambda = \frac{\pi^2}{3}\operatorname{tr}(\boldsymbol{\gamma}_{\mathrm{e}} + \boldsymbol{\gamma}_{\mathrm{m}}). \tag{2.11}$$

An interesting variational result based on (2.11) states that among all isotropic, homogeneous scatterers of equal volume and susceptibilities, the spherical scatterer minimizes the averaged integrated extinction [10, Thm. 3].

3 Bounds on broadband scattering

The main result of Section 2.2, (2.8), is now exploited. Firstly, upper and lower bounds on the integrated extinction utilizing the eigenvalue properties of the polarizability dyadics are established. These estimates are followed by two additional upper and lower bounds based on the results of Jones [10, 11].

3.1 Eigenvalue estimates

Since the extinction cross section is non-negative, it is clear that for any wavelength interval $\Lambda \subset [0, \infty)$,

$$|\Lambda| \min_{\lambda \in \Lambda} \sigma(\lambda) \leq \int_\Lambda \sigma(\lambda)\ \mathrm{d}\lambda \leq \int_0^\infty \sigma_{\mathrm{ext}}(\lambda)\ \mathrm{d}\lambda, \tag{3.1}$$

where $|\Lambda|$ is the absolute bandwidth and σ denotes any of the extinction, scattering and absorption cross sections σ_{ext}, σ_{s}, and σ_{a}, respectively.

The static polarizability dyadics $\boldsymbol{\gamma}_{\mathrm{e}}$ and $\boldsymbol{\gamma}_{\mathrm{m}}$ are real-valued and symmetric, and hence diagonalizable with real-valued eigenvalues $\gamma_{\mathrm{e}j}$ and $\gamma_{\mathrm{m}j}$ with $j = 1, 2, 3$, respectively, ordered as $\gamma_{\mathrm{e}1} \geq \gamma_{\mathrm{e}2} \geq \gamma_{\mathrm{e}3}$ and $\gamma_{\mathrm{m}1} \geq \gamma_{\mathrm{m}2} \geq \gamma_{\mathrm{m}3}$. Since the right hand side of (2.8) is the Rayleigh quotients of $\boldsymbol{\gamma}_{\mathrm{e}}$ and $\boldsymbol{\gamma}_{\mathrm{m}}$, their largest and smallest eigenvalues bound (2.8) according to standard matrix theory,[1] *viz.*,

$$\pi^2(\gamma_{\mathrm{e}3} + \gamma_{\mathrm{m}3}) \leq \int_0^\infty \sigma_{\mathrm{ext}}(\lambda)\ \mathrm{d}\lambda \leq \pi^2(\gamma_{\mathrm{e}1} + \gamma_{\mathrm{m}1}), \tag{3.2}$$

[1] If the eigenvectors corresponding to the largest eigenvalues are the same for the electric and the magnetic cases, the bounds in (3.2) can be sharpened.

Equality on the left (right) hand side of (3.2) holds when $\hat{\boldsymbol{p}}_{\mathrm{e}}$ is a unit eigenvector of $\boldsymbol{\gamma}_{\mathrm{e}}$ with eigenvalue $\gamma_{\mathrm{e}3}$ ($\gamma_{\mathrm{e}1}$) and $\hat{\boldsymbol{p}}_{\mathrm{m}}$ simultaneously is a unit eigenvector of $\boldsymbol{\gamma}_{\mathrm{m}}$ with eigenvalue $\gamma_{\mathrm{m}3}$ ($\gamma_{\mathrm{m}1}$).

3.2 Scatterers of arbitrary shape

Broadband scattering in the sense of the integrated extinction is according to (3.2) directly related to the eigenvalues of the static polarizability dyadics. Lemma 2 in Jones [11] applied to (3.2) yields

$$\pi^2 \int_V \frac{\chi_{\mathrm{e}}(\boldsymbol{x})}{\chi_{\mathrm{e}}(\boldsymbol{x})+1} + \frac{\chi_{\mathrm{m}}(\boldsymbol{x})}{\chi_{\mathrm{m}}(\boldsymbol{x})+1} \ \mathrm{dV}_{\boldsymbol{x}} \leq \int_0^\infty \sigma_{\mathrm{ext}}(\lambda) \ \mathrm{d}\lambda \leq \pi^2 \int_V \chi_{\mathrm{e}}(\boldsymbol{x}) + \chi_{\mathrm{m}}(\boldsymbol{x}) \ \mathrm{dV}_{\boldsymbol{x}}. \tag{3.3}$$

The bounds in (3.3) are sharp in the sense that equality can be obtained as a limiting process for certain homogeneous ellipsoids, see Section 4.

The right hand side of (3.3) is bounded from above by $|V|\|\chi_{\mathrm{e}}+\chi_{\mathrm{m}}\|_\infty$, where $\|f\|_\infty = \sup_{\boldsymbol{x}\in V}|f(\boldsymbol{x})|$ denotes the supremum norm. As a consequence, the upper bound on the integrated extinction for any heterogeneous scatterer is less than or equal to the integrated extinction for the corresponding homogeneous scatterer with susceptibilities $\|\chi_{\mathrm{e}}\|_\infty$ and $\|\chi_{\mathrm{m}}\|_\infty$. This observation leads to the conclusion that there is no fundamental difference on the integrated extinction between scattering by heterogeneous and homogeneous obstacles.

For weak scatterers in the sense of the Born-approximation, $\|\chi_{\mathrm{e}}+\chi_{\mathrm{m}}\|_\infty \ll 1$, and (3.3) implies

$$\int_0^\infty \sigma_{\mathrm{ext}}(\lambda) \ \mathrm{d}\lambda = \pi^2 \int_V \chi_{\mathrm{e}}(\boldsymbol{x}) + \chi_{\mathrm{m}}(\boldsymbol{x}) \ \mathrm{dV}_{\boldsymbol{x}} + \mathcal{O}(\|\chi_{\mathrm{e}}+\chi_{\mathrm{m}}\|_\infty^2), \tag{3.4}$$

where the Taylor series expansion $1/(1+x) = 1+\mathcal{O}(x)$ for $|x|<1$ have been used. Note that (3.4) reduces to a particularly simple form for homogeneous scatterers.

3.3 Star-shaped scatterers

Due to (2.9), it is possible to derive upper bounds on the integrated extinction by applying the bounds to the corresponding homogeneous scatterer with susceptibilities $\|\chi_{\mathrm{e}}\|_\infty$ and $\|\chi_{\mathrm{m}}\|_\infty$. To this end, assume V is star-shaped in the sense that $K_V \neq \emptyset$, where K_V is the set of $\boldsymbol{x} \in V$ such that for all $\boldsymbol{y} \in V$ and $0 \leq s \leq 1$ the straight line $\boldsymbol{x}+(1-s)\boldsymbol{y}$ is contained in V, *i.e.*, if it has an interior point from which its entire boundary can be seen. For a convex scatterer, $K_V = V$.

A refined upper bound on $\gamma_{\mathrm{e}1}$ and $\gamma_{\mathrm{m}1}$ [10, Thm. 5] applied to (3.2), also taking into account the shape of V, yields the inequality

$$\int_0^\infty \sigma_{\mathrm{ext}}(\lambda) \ \mathrm{d}\lambda \leq \pi^2|V|\psi\left(\frac{\|\chi_{\mathrm{e}}\|_\infty}{\psi+\|\chi_{\mathrm{e}}\|_\infty} + \frac{\|\chi_{\mathrm{m}}\|_\infty}{\psi+\|\chi_{\mathrm{m}}\|_\infty}\right), \tag{3.5}$$

where the geometrical factor ψ is defined by

$$\psi = \frac{3}{|V|}\max_j \int_S \frac{(\hat{\boldsymbol{e}}_j \cdot \boldsymbol{r})^2}{\boldsymbol{r}\cdot\hat{\boldsymbol{\nu}}} \ \mathrm{dS}_{\boldsymbol{r}} \leq \frac{9}{|V|}\int_S \frac{r^2}{\boldsymbol{r}\cdot\hat{\boldsymbol{\nu}}} \ \mathrm{dS}_{\boldsymbol{r}}. \tag{3.6}$$

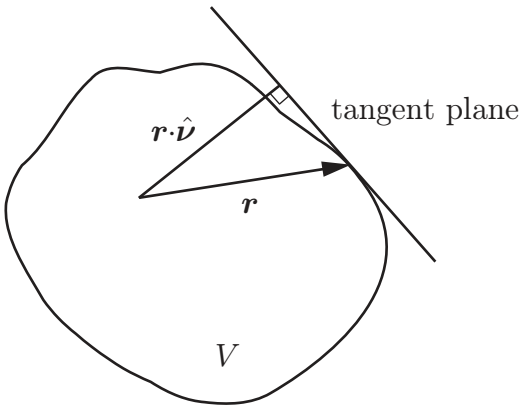

Figure 3: Geometry for the star-shape parametrization.

Here, $\hat{\boldsymbol{e}}_j$ denote mutually orthonormal vectors and $\mathrm{dS}_{\boldsymbol{r}}$ denotes the surface measure of S with respect to $\boldsymbol{r}$ (S is the bounding surface of V). The denominator in (3.6) is the distance from the tangent plane to the origin, see Figure 3. The upper bound in (3.6) is independent of the coordinate system orientation but depends on the location of the origin.

Furthermore, the right hand side of (3.5) is bounded from above by either $\|\chi_{\mathrm{e}}\|_\infty$ and $\|\chi_{\mathrm{m}}\|_\infty$ or ψ. The first case yields (3.3) for a homogeneous scatterer (material parameters $\|\chi_{\mathrm{e}}\|_\infty$ and $\|\chi_{\mathrm{m}}\|_\infty$), while the latter implies

$$\int_0^\infty \sigma_{\mathrm{ext}}(\lambda)\ \mathrm{d}\lambda \leq 2\pi^2|V|\psi, \tag{3.7}$$

irrespectively of the material parameters of V. By comparing (3.3) with (3.7), it is clear that (3.7) provides the sharpest bound when $2\psi < \|\chi_{\mathrm{e}} + \chi_{\mathrm{m}}\|_\infty$. Note that (2.9) implies that it is possible to evaluate (3.6) for any surface circumscribing the scatterer V.

The geometrical factor for the oblate spheroid is $\psi = 3(4+\xi^{-2})/5$ and for the prolate spheroid $\psi = 3(3+2\xi^{-2})/5$ (the origin at the center of the spheroid), where $\xi \in [0,1]$ is the ratio of the minor to the major semi-axis. In particular, $\psi = 3$ for the sphere. The bound in (3.5) is isoperimetric since equality holds for the homogeneous sphere, see Section 4. The geometrical factor ψ for the circular cylinder of radius b and length ℓ is[2] $\psi = \max\{3+3b^2/\ell^2, 3+\ell^2/2b^2\}$.

3.4 Jung's theorem

Jung's theorem [13] gives an optimal upper bound on the radius of a bounded subset $V \subset \mathbb{R}^3$ in terms of its diameter, $\operatorname{diam} V$. The theorem states that V is contained in the unique sphere of radius $R_V \leq \sqrt{6}/4 \operatorname{diam} V$, with equality if and only if the closure of V contains the vertices of a tetrahedron of edge lengths equal to $\operatorname{diam} V$.

[2] This expression deviates from the result of Jones [10].

Since $\psi = 3$ for the sphere and $|V|$ is bounded from above by the volume of the sphere of radius R_V, (3.5) yields

$$\int_0^\infty \sigma_{\text{ext}}(\lambda)\ \mathrm{d}\lambda \leq \frac{\pi^3 3\sqrt{6}}{8}(\operatorname{diam} V)^3 \left(\frac{\|\chi_{\text{e}}\|_\infty}{3+\|\chi_{\text{e}}\|_\infty} + \frac{\|\chi_{\text{m}}\|_\infty}{3+\|\chi_{\text{m}}\|_\infty} \right). \tag{3.8}$$

The right hand side of (3.8) can be estimated from above independently of the material parameters. We get

$$\int_0^\infty \sigma_{\text{ext}}(\lambda)\ \mathrm{d}\lambda \leq \frac{\pi^3 3\sqrt{6}}{4}(\operatorname{diam} V)^3,$$

which is useful in cases where the right hand side of (3.7) diverges.

In this section, we have applied Jung's theorem to a sphere circumscribing the scatterer. There are, however, other choices of circumscribing surfaces that can be utilized [9].

4 Homogeneous ellipsoidal scatterers

For homogeneous, anisotropic ellipsoidal scatterers with susceptibility dyadics $\boldsymbol{\chi}_{\text{e}}$ and $\boldsymbol{\chi}_{\text{m}}$, closed-form expressions of $\boldsymbol{\gamma}_{\text{e}}$ and $\boldsymbol{\gamma}_{\text{m}}$ exist [12], *viz.*,

$$\boldsymbol{\gamma}_i = |V|\boldsymbol{\chi}_i \cdot (\mathbf{I} + \mathbf{L}\cdot\boldsymbol{\chi}_i)^{-1}, \quad i = \text{e}, \text{m} \tag{4.1}$$

where $\mathbf{L}$ and $\mathbf{I}$ are the depolarizing and unit dyadics in $\mathbb{R}^3$, respectively. In terms of the semi-axes a_j in the $\hat{\boldsymbol{e}}_j$-direction, the volume $|V| = 4\pi a_1 a_2 a_3/3$. The depolarizing dyadic has unit trace, and is real-valued and symmetric [30], and, hence, diagonalizable with real-valued eigenvalues. Its eigenvalues are the depolarizing factors L_j [6, 23]

$$L_j = \frac{a_1 a_2 a_3}{2} \int_0^\infty \frac{\mathrm{d}s}{(s+a_j^2)\sqrt{(s+a_1^2)(s+a_2^2)(s+a_3^2)}}, \quad j = 1, 2, 3. \tag{4.2}$$

The depolarization factors satisfy $0 \leq L_j \leq 1$ and $\sum_j L_j = 1$.

Closed-form expressions of (4.2) exist in the special case of the ellipsoids of revolution, *i.e.*, the prolate and oblate spheroids. In terms of the eccentricity $e = \sqrt{1-\xi^2}$, where $\xi \in [0,1]$ is the ratio of the minor to the major semi-axis, the depolarizing factors are (symmetry axis along the $\hat{\boldsymbol{e}}_3$-direction)

$$L_1 = L_2 = \frac{1}{4e^3}\left(2e - (1-e^2)\ln\frac{1+e}{1-e}\right), \qquad L_3 = \frac{1-e^2}{2e^3}\left(\ln\frac{1+e}{1-e} - 2e\right), \tag{4.3}$$

and

$$L_1 = L_2 = \frac{1-e^2}{2e^2}\left(-1 + \frac{\arcsin e}{e\sqrt{1-e^2}}\right), \qquad L_3 = \frac{1}{e^2}\left(1 - \frac{\sqrt{1-e^2}}{e}\arcsin e\right),$$

for the prolate and oblate spheroids, respectively. In particular, $L_j = 1/3$ for the sphere.

The integrated extinction for anisotropic homogeneous ellipsoidal scatterers is given by (4.1) inserted into (2.8). The result is

$$\int_0^\infty \sigma_{\text{ext}}(\lambda)\ \mathrm{d}\lambda = \pi^2|V| \sum_{i=\text{e,m}} \hat{\boldsymbol{p}}_i^* \cdot \boldsymbol{\chi}_i \cdot (\mathbf{I} + \mathbf{L} \cdot \boldsymbol{\chi}_i)^{-1} \cdot \hat{\boldsymbol{p}}_i. \tag{4.4}$$

For isotropic material parameters, $\boldsymbol{\chi}_\text{e} = \chi_\text{e}\mathbf{I}$ and $\boldsymbol{\chi}_\text{m} = \chi_\text{m}\mathbf{I}$, (4.4) reduces to

$$\int_0^\infty \sigma_{\text{ext}}(\lambda)\ \mathrm{d}\lambda = \pi^2|V| \sum_{j=1}^{3} \left(\frac{\kappa_{\text{e}j}\chi_\text{e}}{1 + \chi_\text{e}L_j} + \frac{\kappa_{\text{m}j}\chi_\text{m}}{1 + \chi_\text{m}L_j} \right), \tag{4.5}$$

where $\kappa_{\text{e}j} = |\hat{\boldsymbol{p}}_\text{e} \cdot \hat{\boldsymbol{e}}_j|^2$ and $\kappa_{\text{m}j} = |\hat{\boldsymbol{p}}_\text{m} \cdot \hat{\boldsymbol{e}}_j|^2$ are the polarization vectors projected onto the mutually orthonormal vectors $\hat{\boldsymbol{e}}_j$. Note that $\sum_j \kappa_{\text{e}j} = \sum_j \kappa_{\text{m}j} = 1$, and that the averaged integrated extinction is characterized by $\kappa_{\text{e}j} = \kappa_{\text{m}j} = 1/3$. For prolate and oblate spheroids, which are axially symmetric with respect to the $\hat{\boldsymbol{e}}_3$-axis, a plane wave incident at an angle θ to this axis, yields

$$\begin{cases} \kappa_{\text{e}1} + \kappa_{\text{e}2} = 1 \\ \kappa_{\text{e}3} = 0 \\ \kappa_{\text{m}1} + \kappa_{\text{m}2} = \cos^2\theta \\ \kappa_{\text{m}3} = \sin^2\theta \end{cases} \quad \text{(TE)} \qquad \begin{cases} \kappa_{\text{m}1} + \kappa_{\text{m}2} = 1 \\ \kappa_{\text{m}3} = 0 \\ \kappa_{\text{e}1} + \kappa_{\text{e}2} = \cos^2\theta \\ \kappa_{\text{e}3} = \sin^2\theta \end{cases} \quad \text{(TM)}$$

In the limit as the volume goes to zero, the integrated extinction vanishes for a scatterer with finite susceptibilities. To obtain a non-zero integrated extinction, the scatterer has to be conducting, see *e.g.*, the PEC disk below. In the long wavelength PEC limit, see (2.10), the integrated extinction becomes

$$\int_0^\infty \sigma_{\text{ext}}(\lambda)\ \mathrm{d}\lambda = \pi^2|V| \sum_{j=1}^{3} \left(\frac{\kappa_{\text{e}j}}{L_j} - \frac{\kappa_{\text{m}j}}{1 - L_j} \right). \tag{4.6}$$

The right hand side of (4.5) is bounded from above by χ_i and from below by $\chi_i/(1+\chi_i)$. The bounds in (3.3) are sharp in the sense that χ_i and $\chi_i/(1+\chi_i)$ are obtained at arbitrary precision for the infinite needle and disk of constant volume $|V|$, respectively. In fact, the upper bound holds for an infinite needle oriented along the $\hat{\boldsymbol{e}}_3$-direction ($L_1 + L_2 = 1$) with parallel polarization ($\kappa_{i3} = 1$). The corresponding equality for the lower bound holds for the infinite disk with unit normal vector $\hat{\boldsymbol{e}}_3$ ($L_3 = 1$) with parallel polarization ($\kappa_{i3} = 1$).

A simple example of (4.5) is given by the homogeneous sphere for which the integrated extinction is equal to $3\pi^2|V| \sum_i \chi_i/(\chi_i+3)$ independent of $\kappa_{\text{e}j}$ and $\kappa_{\text{m}j}$, which also is the result of Bohren and Huffman for the non-magnetic case [4, p. 117]. In particular, the PEC limit (2.10) implies that the integrated extinction for the sphere is equal to $3\pi^2|V|/2$. Similar results for stratified dielectric spheres are obtained using recursive compositions of Möbius transformations. For the case of two layers, see Section 5.5.

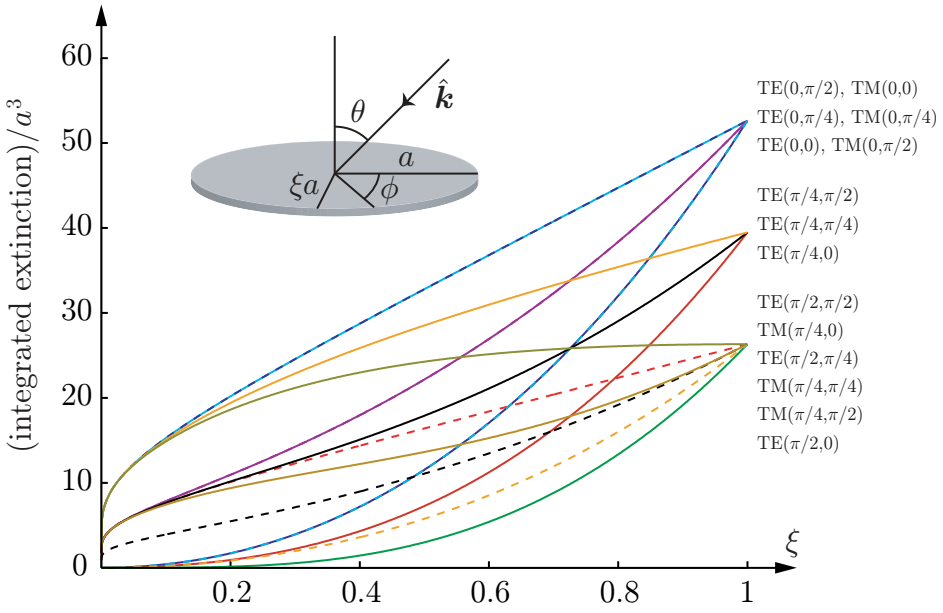

Figure 4: The integrated extinction (4.7) in units of a^3 as function of the semi-axis ratio ξ for the PEC elliptic disk. The notations $\mathrm{TE}(\theta,\phi)$ and $\mathrm{TM}(\theta,\phi)$ refer to the TE- and TM-polarizations for $\theta,\phi \in \{0,\pi/4,\pi/2\}$.

The integrated extinction for the PEC elliptic disk is given by (4.6), and the integrals in (4.2), as the semi-axis a_3 approaches zero, are available in the literature [6, p. 507], [23]. The result is

$$\begin{cases} L_1/|V| = \dfrac{3}{4\pi a^3 e^2}\,(\mathrm{K}-\mathrm{E}) \\ L_2/|V| = \dfrac{3}{4\pi a^3 e^2}\,\big(\mathrm{E}/(1-e^2)-\mathrm{K}\big) \\ (L_3-1)/|V| = -\dfrac{3\mathrm{E}}{4\pi a^3(1-e^2)} \end{cases}$$

where a is the major semi-axis, and where $\mathrm{E}=\mathrm{E}(e^2)$ and $\mathrm{K}=\mathrm{K}(e^2)$ are the complete elliptic integrals of first and second kind, respectively [1, p. 590]. We obtain

$$\int_0^\infty \sigma_{\mathrm{ext}}(\lambda)\ \mathrm{d}\lambda = \frac{4\pi^3 a^3}{3} \begin{cases} B\cos^2\phi + C\sin^2\phi - A\sin^2\theta & \mathrm{TE} \\ \big(B\sin^2\phi + C\cos^2\phi\big)\cos^2\theta & \mathrm{TM} \end{cases} \tag{4.7}$$

where θ and ϕ are the spherical angles of the incident direction, $\hat{\boldsymbol{k}}$. The factors A, B, and C are defined as

$$A = \frac{1-e^2}{\mathrm{E}}, \quad B = \frac{e^2(1-e^2)}{\mathrm{E}-(1-e^2)\mathrm{K}}, \quad C = \frac{e^2}{\mathrm{K}-\mathrm{E}}.$$

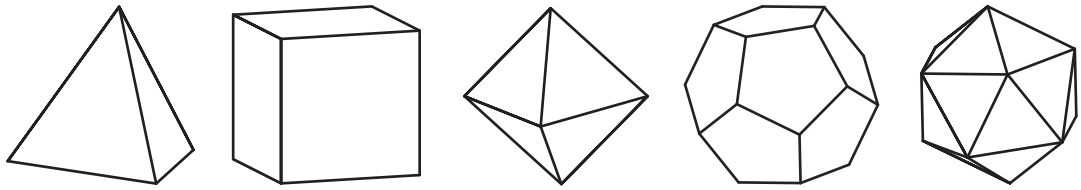

$49.6|V|$ $35.9|V|$ $35.0|V|$ $31.4|V|$ $30.9|V|$

Figure 5: The integrated extinctions for the Platonic solids based on MoM-calculations [25]. The Platonic solids are from left to right the tetrahedron, hexahedron, octahedron, dodecahedron and icosahedron, with 4, 6, 8, 12 and 20 faces, respectively.

Note that the TM-polarization vanishes for $\theta = \pi/2$ independently of $\phi \in [0, 2\pi)$. The integrated extinction (4.7) can also be derived from the long wavelength limit of the T-matrix approach [3].

The integrated extinction in the right hand side of (4.7) as function of ξ is depicted in Figure 4. Note the degeneracy of the integrated extinction at the end points $\xi = 0$ and $\xi = 1$, corresponding to the PEC needle of length $2a$ and the PEC circular disk of radius a, respectively.

5 Numerical results

In this section, we illustrate the theoretical results obtained above by several numerical examples. Specifically, we calculate the extinction cross sections and the eigenvalues of the polarizability dyadics for a set of scatterers with isotropic material parameters. These results are then compared to the theoretical results presented in Sections 2, 3, and 4.

5.1 Platonic solids

Since the homogeneous Platonic solids are invariant under a set of appropriate point groups, their polarizability dyadics are isotropic. By (2.8) this implies that the integrated extinctions are independent of both polarization and incident direction. The five Platonic solids are depicted in Figure 5, see also Table 1, together with the integrated extinctions in the non-magnetic, high-contrast limit, *i.e.*, $\chi_{\mathrm{e}} \to \infty$.

A common lower bound on the integrated extinctions in Figure 5 is obtained by (4.5) for the volume-equivalent sphere. This lower bound is motivated by Jones' result [10, Thm. 3], and the fact that the polarizability dyadics are isotropic. The result is $14.80|V|$.

Upper bounds on the integrated extinctions are given by the smallest circumscribing high-contrast spheres, which based on solid geometry are found to be $241.60|V|$, $80.54|V|$, $61.98|V|$, $44.62|V|$ and $48.96|V|$ for the tetrahedron, hexahedron, octahedron, dodecahedron and icosahedron, respectively, see (2.9). The upper

Platonic solids	$\gamma_e/\lvert V\rvert$	γ_e/a^3	**Int. ext.**	$\lvert V\rvert/a^3$
Tetrahedron	5.03	0.593	$49.6\lvert V\rvert$	$\sqrt{2}/12$
Hexahedron	3.64	3.64	$35.9\lvert V\rvert$	1
Octahedron	3.55	1.67	$35.0\lvert V\rvert$	$\sqrt{2}/3$
Dodecahedron	3.18	24.4	$31.4\lvert V\rvert$	$(15+7\sqrt{5})/4$
Icosahedron	3.13	6.83	$30.9\lvert V\rvert$	$5(3+\sqrt{5})/12$

Table 1: The eigenvalues γ_e and the integrated extinction for the Platonic solids in units of $|V|$ in the high-contrast limit $\chi_e \to \infty$. The last column gives the volume of the Platonic solids expressed in the edge length a.

and lower bounds are seen to be quite close to the numerical values presented in Figure 5, at least for the dodecahedron and icosahedron, which do not deviate much from the volume-equivalent sphere. Since the Platonic solids are star-shaped with respect to all interior points, a somewhat different set of upper bounds can be derived from (3.5).

5.2 Dielectric spheroids

The averaged extinction cross section, $\bar{\sigma}_{\text{ext}}$, as function of the radius ka for a prolate and oblate spheroid is illustrated in Figure 6. The solid curve depicts the averaged extinction cross section (equal to the extinction cross section) for the volume-equivalent sphere of radius a, and the dashed and dotted curves correspond to the prolate and oblate spheroids, respectively, of semi-axis ratio $\xi = 1/2$. The scatterers are non-magnetic with electric susceptibility $\chi_e = 1$. Note that the largest variation of the curves in Figure 6 occurs for the sphere due to the fact that its extinction cross section is independent of the polarization and the direction of incidence, which implies that no resonances are averaged out in contrast to the case for the prolate and oblate spheroids.

The numerically integrated averaged extinction cross sections for $ka \in [0, 20]$ agree within relative errors of 1.2% with the theoretical values $7.46|V|$ and $7.48|V|$ based on (4.5) for the prolate and oblate spheroids, respectively. The corresponding values for the sphere are 0.7% and $7.40|V|$. The calculations are based on the T-matrix approach [19].

According to Section 2, a lower bound on the averaged integrated extinctions for the spheroids is $7.40|V|$ corresponding to the volume-equivalent sphere. Based on (3.3), lower and upper bounds common to the three curves in Figure 6 are $4.93|V|$ and $9.87|V|$, respectively. Using the star-shaped bound (3.5), these upper bounds are improved to $8.57|V|$ and $8.17|V|$ for the prolate and the oblate spheroids, respectively. Both the lower and upper bounds are reasonable close to the theoretical values.

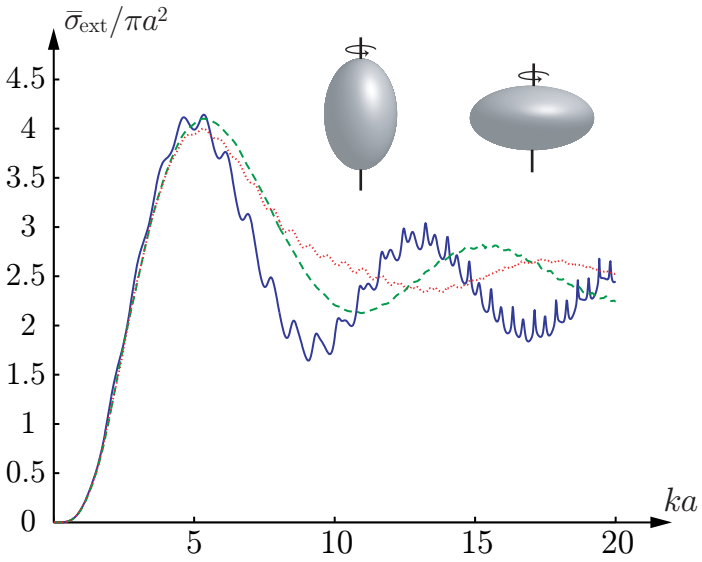

Figure 6: The averaged extinction cross section, $\bar{\sigma}_{\text{ext}}$, in units of πa^2 as function of ka for a prolate (dashed) and oblate (dotted) non-magnetic spheroid with electric susceptibility $\chi_{\text{e}} = 1$ and semi-axis ratio $\xi = 1/2$. The extinction cross section for the volume-equivalent sphere of radius a (solid) is included.

5.3 Lorentz dispersive circular cylinder

The averaged extinction cross section, $\bar{\sigma}_{\text{ext}}$, as function of the frequency for a Lorentz dispersive circular cylinder is depicted in Figure 7. The ratio of the cylinder length ℓ to its radius b is $\ell/b = 2$. The cylinder is non-magnetic with electric susceptibility given by the Lorentz model [4, Sec. 9.1]

$$\chi_{\text{e}}(\omega) = \frac{\omega_{\text{p}}^2}{\omega_0^2 - \omega^2 - \mathrm{i}\omega\nu},$$

where ω_{p} is the plasma frequency, ν the collision frequency and ω_0 the resonance frequency. Explicit values of ω_{p}, ω_0 and ν are $\omega_{\text{p}} = \omega_0 = 4\pi \cdot 10^9\,\text{rad/s}$, $\nu = 0.7 \cdot 10^9\,\text{rad/s}$, and $\omega_{\text{p}} = \omega_0 = 20\pi \cdot 10^9\,\text{rad/s}$, $\nu = 10^{10}\,\text{rad/s}$, respectively. The Lorentz parameters are chosen such that all three curves in the left figure have the same long wavelength susceptibility $\chi_{\text{e}} = \chi_{\text{e}}(0) = 1$. The first two curves with peaks at 2 GHz and 10 GHz depict the dispersive case, while the third for comparison illustrates the results for the non-dispersive case. The three curves in the left figure have the same integrated extinctions, since their long wavelength susceptibilities coincide. The calculation is based on the T-matrix approach [19].

A numerical calculation of the eigenvalues of the polarizability dyadic for the dielectric cylinder is performed by adopting the finite element method (FEM). The results are $0.773|V|$, $0.749|V|$, and $0.749|V|$. This result implies that the numerically computed averaged extinction cross section, $\bar{\sigma}_{\text{ext}}$, in (2.11) is $7.47|V|$. The numerically calculated integrated extinction in the interval $f \in [0, 70]\,\text{GHz}$ is $7.43|V|$ for the first, and $7.44|V|$ for the second curve in Figure 7.

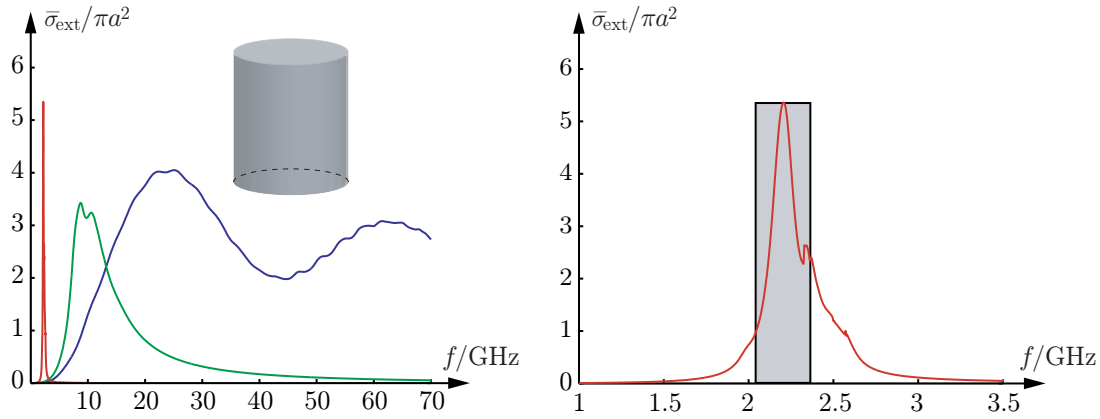

Figure 7: The averaged extinction cross section, $\bar{\sigma}_{\text{ext}}$, in units of πa^2 as function of the frequency in GHz for a non-magnetic Lorentz dispersive circular cylinder with volume-equivalent sphere of radius $a = 1\,\text{cm}$. The three curves in the left figure have the same long wavelength response $\chi_{\text{e}} = 1$. The first two curves with peaks at 2 GHz and 10 GHz are Lorentz dispersive, while the third curve is non-dispersive. The right figure is a close-up of the 2 GHz peak in the left figure.

Common lower and upper bounds on the integrated extinctions based on (3.3) are $4.94|V|$ and $9.87|V|$, respectively. A sharper lower bound is $7.40|V|$ corresponding to the volume-equivalent sphere. An upper bound can for comparison be obtained from (3.5). For $\ell/b = 2$ this implies $\psi = 5$ and the upper bound $8.23|V|$, which is sharper than the bound based on (3.3).

The figure on the right hand side of Figure 7 is a close-up of the 2 GHz peak. The boundary curve of the box corresponds to an artificial scatterer with averaged extinction cross section supported at the peak, *i.e.*, for an averaged extinction cross section that vanishes everywhere outside the box. The integrated extinction for the boundary curve of the box and the three curves in the left hand side of Figure 7 coincide.

5.4 Debye dispersive non-spherical raindrop

The averaged extinction cross section, $\bar{\sigma}_{\text{ext}}$, as function of the frequency for a falling raindrop is depicted in Figure 8.

The axially symmetric drop depicted in Figure 8 is parameterized by the polar angle θ and the radial distance

$$r(\theta) = r_0 \left(1 + \sum_{k=0}^{10} c_k \cos k\theta \right),$$

where r_0 is determined from the condition of the volume-equivalence with the sphere of radius a, *i.e.*, $|V| = \frac{2\pi}{3} \int_0^\pi r^3(\theta) \sin\theta \; \mathrm{d}\theta$ with $|V| = 4\pi a^3/3$. The radius of volume-equivalent sphere used in Figure 8 is $a = 2\,\text{mm}$ with associated shape coefficients

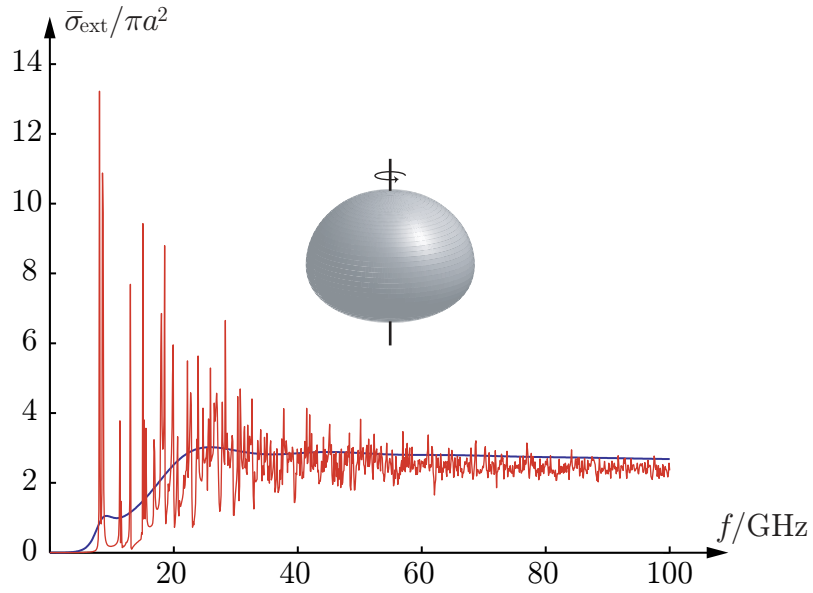

Figure 8: The averaged extinction cross section, $\bar{\sigma}_{\rm ext}$, in units of πa^2 as function of the frequency in GHz for a raindrop of volume-equivalent radius $a = 2\,\text{mm}$. The smooth curve is for the Debye-model (5.1), while the oscillatory curve is for the non-dispersive case. The two curves have the same long wavelength response and therefore also the same integrated extinctions.

$c_0 = -0.0458$, $c_1 = 0.0335$, $c_2 = -0.1211$, $c_3 = 0.0227$, $c_4 = 0.0083$, $c_5 = -0.0089$, $c_6 = 0.0012$, $c_7 = 0.0021$, $c_8 = -0.0013$, $c_9 = -0.0001$ and $c_{10} = 0.0008$ [2]. The calculation is based on the T-matrix approach [19].

The smooth curve is for the non-magnetic Debye model [4, Sec. 9.5]

$$\chi_{\rm e}(\omega) = \chi_\infty + \frac{\chi_{\rm s} - \chi_\infty}{1 - {\rm i}\omega\tau}, \tag{5.1}$$

where τ is the relaxation time and χ_∞ and $\chi_{\rm s}$ are the short and long wavelength susceptibilities, respectively. Pure water at 20°C is considered with $\chi_{\rm s} = 79.2$, $\chi_\infty = 4.6$ and $\tau = 9.36\,\text{ps}$ [14, p. 43]. The curve with largest variation is for the non-dispersive case with an susceptibility identical to the long wavelength limit, $\chi_{\rm s}$, of (5.1).

Since the long wavelength susceptibilities coincide for the two curves in Figure 8, their integrated extinctions are equal according to (2.11). The eigenvalues of the polarizability dyadics for the raindrop can be obtained by numerical computations. A finite element method (FEM) computation gives the three eigenvalues: $2.43|V|$, $3.21|V|$, and $3.21|V|$, respectively. This result implies that the numerically computed averaged extinction cross section, $\bar{\sigma}_{\rm ext}$, in (2.11) is $29.1|V|$. If we numerically integrate the average extinction cross section in Figure 8 over $f \in [0, 100]\,\text{GHz}$, we get $26.4|V|$ for the dispersive and $25.6|V|$ for the non-dispersive curve, respectively. The reason why the numerically integrated extinctions are about 10% below the FEM values is due to the finite integration interval.

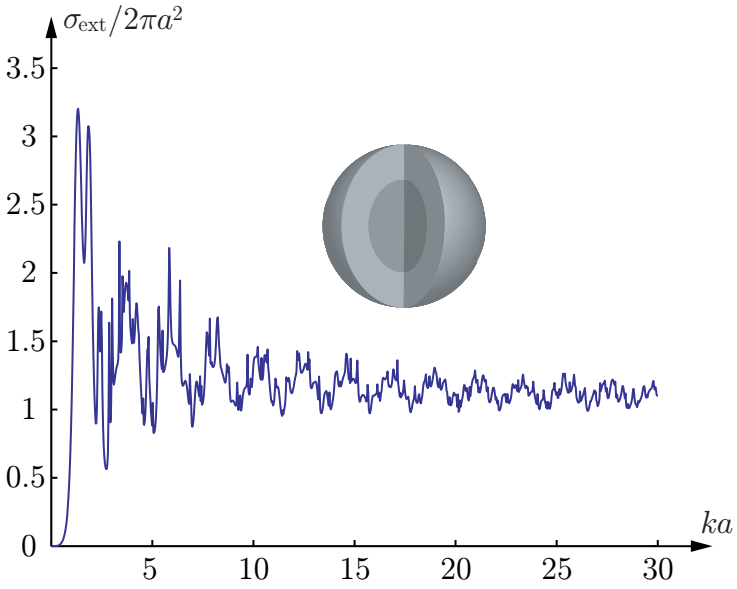

Figure 9: The extinction cross section, σ_{ext}, in units of $2\pi a^2$ as function of the radius ka for a dielectric stratified sphere with two layers of equal volume. The electric and magnetic susceptibilities are $\chi_{\text{e}1} = 2$ and $\chi_{\text{m}1} = 1$ for the core and $\chi_{\text{e}2} = 1$ and $\chi_{\text{m}2} = 2$ for the outer layer.

Lower and upper bounds on the integrated extinctions, given by (3.3), are $9.75|V|$ and $782|V|$, respectively, which are rather crude. A more accurate lower bound is given by the non-magnetic, volume-equivalent sphere with static susceptibilities $\chi_{\text{e}} = \chi_{\text{s}}$, for which (4.5) yields $28.5|V|$. The star-shaped bound in Section 3.3 is also applicable. The result for the raindrop is $32.15|V|$. We observe that both the lower and upper bounds approximate the true value very well.

5.5 Dielectric stratified sphere

Due to spherical symmetry, the polarizability dyadics of a stratified sphere are isotropic and easily computed by recursive applications of Möbius transformations. In particular, the integrated extinction for two layers with electric and magnetic susceptibilities $\chi_{\text{e}1}$ and $\chi_{\text{m}1}$ in the core, and $\chi_{\text{e}2}$ and $\chi_{\text{m}2}$ in the outer layer, respectively, is

$$\int_0^\infty \sigma_{\text{ext}}(\lambda)\ \mathrm{d}\lambda = 3\pi^2|V| \sum_{i=\text{e,m}} \frac{\chi_{i2}(\chi_{i1}+2\chi_{i2}+3)+\varsigma^3(2\chi_{i2}+3)(\chi_{i1}-\chi_{i2})}{(\chi_{i2}+3)(\chi_{i1}+2\chi_{i2}+3)+2\varsigma^3\chi_{i2}(\chi_{i1}-\chi_{i2})}, \quad (5.2)$$

where ς is the ratio of the inner to the outer radius. The special cases $\varsigma = 0$ and $\varsigma = 1$ correspond to homogeneous spheres with susceptibilities χ_{i2} and χ_{i1}, respectively, see Section 4. Moreover, both the cases $\chi_{i1} = \chi_{i2}$ and $\chi_{i2} = 0$ yield the homogeneous sphere of susceptibility χ_{i1}, with the volume of the sphere being a fraction ς^3 of the original volume $|V|$ in the latter case.

The extinction cross section, σ_{ext}, as function of the radius ka for the stratified sphere with two layers of equal volume, $\varsigma = 1/\sqrt[3]{2}$, is depicted in Figure 9. The used susceptibilities are $\chi_{\text{e1}} = 2$ and $\chi_{\text{m1}} = 1$ in the core, and $\chi_{\text{e2}} = 1$ and $\chi_{\text{m2}} = 2$ in the outer layer. The calculations are based on the Mie-series approach [18]. Note that the curve in Figure 9 approaches twice the geometrical cross section area in the short wavelength limit. Compare this observation with the extinction paradox [29, pp. 107–108].

The numerically integrated extinction is $19.1|V|$ for $ka \in [0, 30]$ and $19.3|V|$ for $ka \in [0, 100]$, with relative errors of 1.7% and 0.5%, respectively, compared to the theoretical value $19.4|V|$ given by (5.2).

Lower and upper bounds on the integrated extinction based on the inequality in (2.9) are $14.8|V|$ and $23.7|V|$, respectively, corresponding to the volume-equivalent homogeneous sphere with minimal and maximal susceptibilities, $\inf_{\boldsymbol{x}\in V} \chi_i$ and $\sup_{\boldsymbol{x}\in V} \chi_i$, respectively. Note that this upper bound coincides with the one obtained from (3.5), but that both the lower and upper bounds based on (2.9) are sharper than the ones given by (3.3).

5.6 PEC circular disk

The integrated extinction for the PEC circular disk of radius a is given by (4.7) in the limit $\xi \to 1$. The result is

$$\int_0^\infty \sigma_{\text{ext}}(\lambda)\ \mathrm{d}\lambda = \frac{8\pi^2 a^3}{3} \begin{cases} 1 + \cos^2\theta & (\text{TE}) \\ \\ 2\cos^2\theta & (\text{TM}) \end{cases} \tag{5.3}$$

The right hand side of (5.3) can also be derived from the long wavelength limit of the T-matrix approach [16].

The extinction cross section, σ_{ext}, as function of the radius ka for the PEC circular disk is depicted in Figure 10. The notations TE(θ) and TM(θ) refer to the TE- and TM-polarizations, respectively, and the stars denote the short wavelength limit $\cos\theta$ given by the extinction paradox [29, pp. 107–108]. Note the degeneracy of both polarizations for normal incidence, and that the extinction cross section vanishes identically for TM($\pi/2$). The calculation is based on the T-matrix approach [16].

To find the numerically integrated extinctions, the integration interval $ka \in [0, 15]$ does not suffice to get reasonable accuracy. However, by extending the integrand above $ka = 15$ by the expected short wavelength limit, we obtain relative errors of 0.5% compared to the exact results of (5.3).

The bounds discussed in Section 3 are not directly applicable to the PEC circular disk since the disk has zero volume. However, a crude upper bound is obtained by the circumscribing PEC sphere. The result is $1.5\pi^2$, in units of the volume of the circumscribing sphere. Compare this with the exact results of (5.3) in terms of the volume of the circumscribing sphere — the factor 1.5 for the circumscribing sphere is to be compared with $4/\pi \approx 1.27$ at $\theta = 0$ incidence.

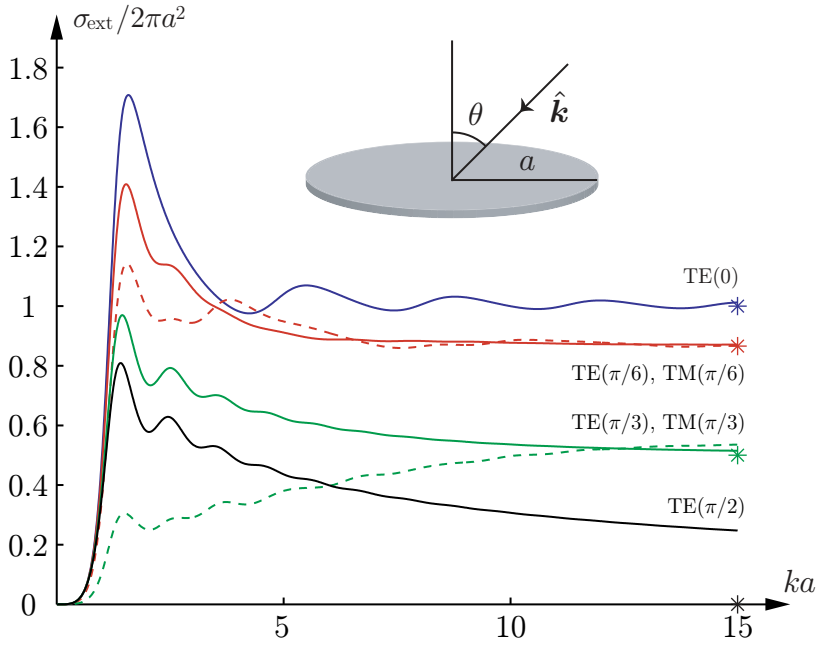

Figure 10: The extinction cross section, σ_{ext}, in units of $2\pi a^2$ as function of the radius ka for the PEC circular disk. The solid and dashed lines are for the TE- and TM-polarizations, respectively, and the stars denote the short wavelength limits $\cos\theta$.

5.7 PEC needle

The integrated extinction for the PEC needle of length $2a$ and oriented along the $\hat{\boldsymbol{e}}_3$-direction is given by (4.3) and (4.6) in the limit $\xi \to 0$. The result is

$$\int_0^\infty \sigma_{\text{ext}}(\lambda)\ \mathrm{d}\lambda = \frac{4\pi^3 a^3}{3} \begin{cases} \mathcal{O}(\xi^2) & \text{(TE)} \\ \dfrac{\sin^2\theta}{\ln 2/\xi - 1} + \mathcal{O}(\xi^2) & \text{(TM)} \end{cases} \tag{5.4}$$

The right hand side of (5.4) can also be derived from the long wavelength limit of the T-matrix approach [3].

The integrated extinction (5.4) is seen to vanish for both polarizations in the limit $\xi \to 0$. Since the extinction cross section is non-negative, this implies that it vanishes almost everywhere except on a set of measure zero consisting of the denumerable resonances for which an integer multiple of $\lambda/2$ coincides with the length of the needle. This result is illustrated numerically in Figure 11, which shows the extinction cross section, σ_{ext}, for the PEC needle for the TM-polarization at normal incidence. Note that, due to symmetry, only resonances corresponding to ka equal to an odd multiple of $\pi/2$ are excited at normal incidence. The numerically integrated extinctions in Figure 11 agree well with (5.4). The relative errors are less than 0.5% with an integration interval $ka \in [0, 12]$ for the three curves.

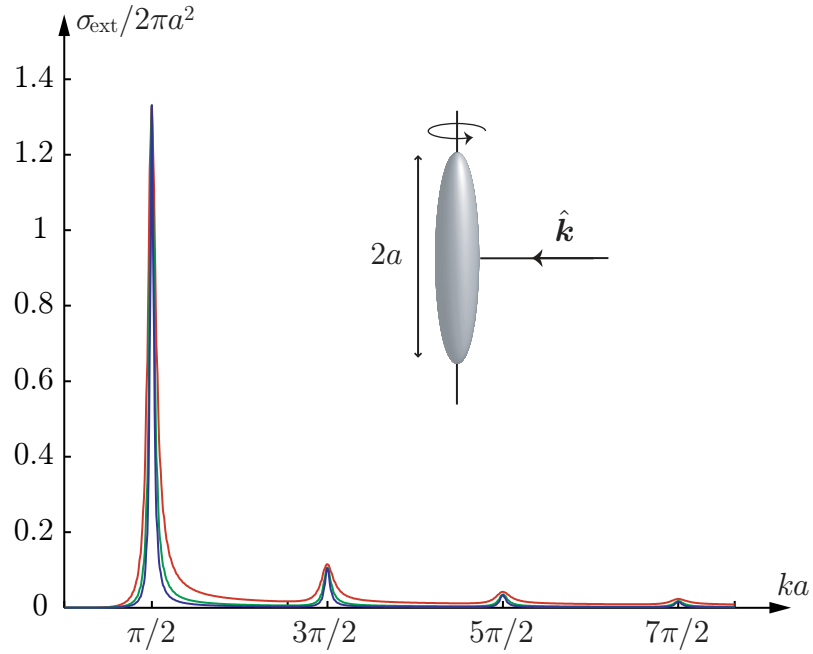

Figure 11: The extinction cross section, σ_{ext}, in units of $2\pi a^2$ as function of ka for the PEC needle of length $2a$. The needle is approximated by a prolate spheroid with semi-axis ratio 10^{-3} for the outermost, 10^{-5} for the intervening, and 10^{-7} for the innermost curve. The calculation is based on the T-matrix approach [3].

6 Concluding remarks

The integrated extinction is an example of what is referred to in modern physics as a dispersion relation [21]. The basic idea for the dispersion relations is that certain linear and causal physical quantities with known high-frequency (short wavelength) asymptotic are boundary values of holomorphic functions of one or more complex variables.

The integrated extinction is particularly important from an antenna point of view, since it generalizes the physical limitations on the antenna performance derived by Chu [5] for the sphere. These new limitations, which can be shown to relate bandwidth and directivity of any antenna in terms of volume and shape, will be reported elsewhere. The integrated extinction is also of great interest in applications to broadband scattering by artificial material models such as metamaterials. In this application, it provides physical limitations on scattering by general material models. Moreover, the bounds presented in Section 3 may be of use to bound material parameters in inverse scattering problems. All these applications to material modeling and inverse scattering problems are currently under investigation, and will be reported in forthcoming papers.

From the perspective of unrealizable physical systems, the derivation of the integrated extinction in Section 2 is similar to the Fano theory [7] of broadband matching. The Fano theory specifies bounds on the amount of power that is possible to

transmit between a transmission line and a load impedance for a given bandwidth. The concept of physical realizability introduced by Fano can be interpreted as a causality condition.

Additional theoretical work on the integrated extinction also includes bi-anisotropy and diamagnetics, which will be reported elsewhere. Finally, it should be noted that the concept of the integrated extinction with minor changes also holds in linear acoustics [15, Sec. 7].

Acknowledgments

The financial support by the Swedish Research Council is gratefully acknowledged.

Appendix A The polarizability dyadics

For an anisotropic scatterer modeled by the material dyadic $\boldsymbol{\tau}$ (electric susceptibility dyadic $\boldsymbol{\chi}_{\mathrm{e}}$ without a conductivity term, or magnetic susceptibility dyadic $\boldsymbol{\chi}_{\mathrm{m}}$), the total electric field $\boldsymbol{E}$ (similarly for the magnetic field $\boldsymbol{H}$) satisfies

$$\begin{cases} \nabla \times \boldsymbol{E}(\boldsymbol{x}) = \boldsymbol{0} \\ \nabla \cdot ((\boldsymbol{\tau}(\boldsymbol{x}) + \mathbf{I}) \cdot \boldsymbol{E}(\boldsymbol{x})) = 0 \end{cases} \quad \boldsymbol{x} \in \mathbb{R}^3$$

Here, $\boldsymbol{\tau}$ is assumed to be a symmetric dyadic at all points $\boldsymbol{x}$ and sufficiently regular to justify the operations below.

Decompose the total field $\boldsymbol{E}$ as $\boldsymbol{E}_j = E_0 \hat{\boldsymbol{e}}_j + \boldsymbol{E}_{\mathrm{s}j}$, where $j = 1, 2, 3$. The pertinent partial differential equation for the scattered field $\boldsymbol{E}_{\mathrm{s}j}$ is then

$$\begin{cases} \nabla \times \boldsymbol{E}_{\mathrm{s}j}(\boldsymbol{x}) = \boldsymbol{0} \\ \nabla \cdot ((\boldsymbol{\tau}(\boldsymbol{x}) + \mathbf{I}) \cdot \boldsymbol{E}_{\mathrm{s}j}(\boldsymbol{x})) = -E_0 \nabla \cdot (\boldsymbol{\tau}(\boldsymbol{x}) \cdot \hat{\boldsymbol{e}}_j) \end{cases} \quad \boldsymbol{x} \in \mathbb{R}^3 \tag{A.1}$$

together with the asymptotic condition $\boldsymbol{E}_{\mathrm{s}j}(\boldsymbol{x}) \to \mathcal{O}(|\boldsymbol{x}|^{-3})$ as $|\boldsymbol{x}| \to \infty$.

The first condition in (A.1) implies that there exists a potential Φ_j related to the scattered field as $\boldsymbol{E}_{\mathrm{s}j} = -\nabla \Phi_j$ satisfying

$$\begin{cases} \nabla \cdot ((\boldsymbol{\tau}(\boldsymbol{x}) + \mathbf{I}) \cdot \nabla \Phi_j(\boldsymbol{x})) = E_0 \nabla \cdot (\boldsymbol{\tau}(\boldsymbol{x}) \cdot \hat{\boldsymbol{e}}_j) \\ \Phi_j(\boldsymbol{x}) \to \mathcal{O}(|\boldsymbol{x}|^{-2}) \text{ as } |\boldsymbol{x}| \to \infty \end{cases} \quad \boldsymbol{x} \in \mathbb{R}^3 \tag{A.2}$$

This problem has a unique solution. The entries of the polarizability dyadic $\boldsymbol{\gamma}$ ($\boldsymbol{\gamma}_{\mathrm{e}}$ or $\boldsymbol{\gamma}_{\mathrm{m}}$ depending on whether the problem is electric or magnetic) is then ($i, j = 1, 2, 3$)

$$\hat{\boldsymbol{e}}_i \cdot \boldsymbol{\gamma} \cdot \hat{\boldsymbol{e}}_j = \frac{1}{E_0} \hat{\boldsymbol{e}}_i \cdot \int_{\mathbb{R}^3} \boldsymbol{\tau}(\boldsymbol{x}) \cdot \boldsymbol{E}_j(\boldsymbol{x}) \, \mathrm{dV}_{\boldsymbol{x}}. \tag{A.3}$$

Scale this solution by a factor α, *i.e.*, let $\boldsymbol{x} \longrightarrow \boldsymbol{x}' = \alpha \boldsymbol{x}$, with material dyadic $\boldsymbol{\tau}'(\boldsymbol{x}') = \boldsymbol{\tau}(\boldsymbol{x})$, and denote the solution to the new problem by $\Phi_j'(\boldsymbol{x}')$. The new

problem then satisfies

$$\begin{cases} \nabla' \cdot \big((\boldsymbol{\tau}'(\boldsymbol{x}') + \mathbf{I}) \cdot \nabla' \Phi_j'(\boldsymbol{x}') \big) = E_0 \nabla' \cdot (\boldsymbol{\tau}'(\boldsymbol{x}') \cdot \hat{\boldsymbol{e}}_j) \\ \Phi_j'(\boldsymbol{x}') \to 0 \text{ as } |\boldsymbol{x}'| \to \infty \end{cases} \quad \boldsymbol{x}' \in \mathbb{R}^3$$

or in the unscaled coordinates

$$\begin{cases} \alpha^{-2} \nabla \cdot \big((\boldsymbol{\tau}(\boldsymbol{x}) + \mathbf{I}) \cdot \nabla \Phi_j'(\alpha \boldsymbol{x}) \big) = E_0 \alpha^{-1} \nabla \cdot (\boldsymbol{\tau}(\boldsymbol{x}) \cdot \hat{\boldsymbol{e}}_j) \\ \Phi_j'(\alpha \boldsymbol{x}) \to 0 \text{ as } |\boldsymbol{x}| \to \infty \end{cases} \quad \boldsymbol{x} \in \mathbb{R}^3$$

Due to the unique solubility of the boundary value problem (A.2), $\Phi_j'(\boldsymbol{x}') = \alpha \Phi_j(\boldsymbol{x})$, and consequently $\boldsymbol{E}_j'(\boldsymbol{x}') = \boldsymbol{E}_j(\boldsymbol{x}) = \boldsymbol{E}_j(\boldsymbol{x}'/\alpha)$. The polarizability dyadic for the scaled problem then becomes

$$\hat{\boldsymbol{e}}_i \cdot \boldsymbol{\gamma}' \cdot \hat{\boldsymbol{e}}_j = \hat{\boldsymbol{e}}_i \cdot \int_{\mathbb{R}^3} \boldsymbol{\tau}'(\boldsymbol{x}') \cdot \boldsymbol{E}_j'(\boldsymbol{x}') \, \mathrm{dV}_{\boldsymbol{x}'} = \alpha^3 \hat{\boldsymbol{e}}_i \cdot \int_{\mathbb{R}^3} \boldsymbol{\tau}(\boldsymbol{x}) \cdot \boldsymbol{E}_j(\boldsymbol{x}) \, \mathrm{dV}_{\boldsymbol{x}},$$

and we see that $\boldsymbol{\gamma}$ scales with the volume $|V| \sim \alpha^3$.

A.1 Symmetry

The polarizability dyadic $\boldsymbol{\gamma}$ is symmetric, since $\boldsymbol{\tau}$ is assumed symmetric at all points $\boldsymbol{x}$. In fact, from (A.3),

$$\hat{\boldsymbol{e}}_i \cdot \boldsymbol{\gamma} \cdot \hat{\boldsymbol{e}}_j = \hat{\boldsymbol{e}}_i \cdot \int_{\mathbb{R}^3} \boldsymbol{\tau}(\boldsymbol{x}) \cdot \hat{\boldsymbol{e}}_j \, \mathrm{dV}_{\boldsymbol{x}} - \frac{1}{E_0} \hat{\boldsymbol{e}}_i \cdot \int_{\mathbb{R}^3} \boldsymbol{\tau}(\boldsymbol{x}) \cdot \nabla \Phi_j(\boldsymbol{x}) \, \mathrm{dV}_{\boldsymbol{x}}. \tag{A.4}$$

The last integral in (A.4) is rewritten as

$$\begin{aligned} &\hat{\boldsymbol{e}}_i \cdot \int_{\mathbb{R}^3} \boldsymbol{\tau}(\boldsymbol{x}) \cdot \nabla \Phi_j(\boldsymbol{x}) \, \mathrm{dV}_{\boldsymbol{x}} \\ &= \int_{\mathbb{R}^3} \nabla \cdot (\hat{\boldsymbol{e}}_i \cdot \boldsymbol{\tau}(\boldsymbol{x}) \Phi_j(\boldsymbol{x})) \, \mathrm{dV}_{\boldsymbol{x}} - \int_{\mathbb{R}^3} \nabla \cdot (\hat{\boldsymbol{e}}_i \cdot \boldsymbol{\tau}(\boldsymbol{x})) \, \Phi_j(\boldsymbol{x}) \, \mathrm{dV}_{\boldsymbol{x}} \\ &= - \int_{\mathbb{R}^3} \nabla \cdot (\boldsymbol{\tau}(\boldsymbol{x}) \cdot \hat{\boldsymbol{e}}_i) \, \Phi_j(\boldsymbol{x}) \, \mathrm{dV}_{\boldsymbol{x}} \\ &= -\frac{1}{E_0} \int_{\mathbb{R}^3} \nabla \cdot ((\boldsymbol{\tau}(\boldsymbol{x}) + \mathbf{I}) \cdot \nabla \Phi_i(\boldsymbol{x})) \, \Phi_j(\boldsymbol{x}) \, \mathrm{dV}_{\boldsymbol{x}}, \end{aligned}$$

due to (A.2) provided $\boldsymbol{\tau}$ is symmetric at all points $\boldsymbol{x}$. Furthermore,

$$\begin{aligned} &\hat{\boldsymbol{e}}_i \cdot \int_{\mathbb{R}^3} \boldsymbol{\tau}(\boldsymbol{x}) \cdot \nabla \Phi_j(\boldsymbol{x}) \, \mathrm{dV}_{\boldsymbol{x}} \\ &= -\frac{1}{E_0} \int_{\mathbb{R}^3} \nabla \cdot \{ ((\boldsymbol{\tau}(\boldsymbol{x}) + \mathbf{I}) \cdot \nabla \Phi_i(\boldsymbol{x})) \, \Phi_j(\boldsymbol{x}) \} \, \mathrm{dV}_{\boldsymbol{x}} \\ &+ \frac{1}{E_0} \int_{\mathbb{R}^3} \nabla \Phi_j(\boldsymbol{x}) \cdot ((\boldsymbol{\tau}(\boldsymbol{x}) + \mathbf{I}) \cdot \nabla \Phi_i(\boldsymbol{x})) \, \mathrm{dV}_{\boldsymbol{x}} \\ &= \frac{1}{E_0} \int_{\mathbb{R}^3} \nabla \Phi_j(\boldsymbol{x}) \cdot ((\boldsymbol{\tau}(\boldsymbol{x}) + \mathbf{I}) \cdot \nabla \Phi_i(\boldsymbol{x})) \, \mathrm{dV}_{\boldsymbol{x}}. \end{aligned}$$

The polarizability dyadic (A.4) therefore becomes

$$\hat{\boldsymbol{e}}_i \cdot \boldsymbol{\gamma} \cdot \hat{\boldsymbol{e}}_j = \hat{\boldsymbol{e}}_i \cdot \int_{\mathbb{R}^3} \boldsymbol{\tau}(\boldsymbol{x}) \cdot \hat{\boldsymbol{e}}_j \, \mathrm{dV}_{\boldsymbol{x}} - \frac{1}{E_0^2} \int_{\mathbb{R}^3} \nabla\Phi_j(\boldsymbol{x}) \cdot ((\boldsymbol{\tau}(\boldsymbol{x}) + \mathbf{I}) \cdot \nabla\Phi_i(\boldsymbol{x})) \, \mathrm{dV}_{\boldsymbol{x}},$$

which clearly is symmetric in the indices i and j if $\boldsymbol{\tau}$ is symmetric at all points $\boldsymbol{x}$.

A.2 High-contrast limit

In the high-contrast limit, when the entries of the material dyadic become infinitely large independent of $\boldsymbol{x}$, the appropriate surface integral representation of the polarizability dyadic is [15, p. 22]

$$\hat{\boldsymbol{e}}_i \cdot \boldsymbol{\gamma} \cdot \hat{\boldsymbol{e}}_j = \frac{1}{E_0} \hat{\boldsymbol{e}}_i \cdot \sum_{n=1}^{N} \int_{S_n} (\hat{\boldsymbol{\nu}}(\boldsymbol{x}) \Phi_j(\boldsymbol{x}) - \boldsymbol{x} \hat{\boldsymbol{\nu}}(\boldsymbol{x}) \cdot \nabla\Phi_j(\boldsymbol{x})) \, \mathrm{dS}_{\boldsymbol{x}},$$

where S_n, $n = 1, 2, \ldots, N$ denote the bounding surfaces (outward-directed unit normal $\hat{\boldsymbol{\nu}}$) of the domain outside the material (we assume that $\boldsymbol{\tau}$ is compactly supported). Moreover, $\Psi_j(\boldsymbol{x}) = \Phi_j(\boldsymbol{x}) - E_0 x_j$, is the solution to ($n = 1, 2, \ldots, N$)

$$\begin{cases} \nabla^2 \Psi_j(\boldsymbol{x}) = 0, \quad \boldsymbol{x} \text{ outside } S_n \\ \displaystyle\int_{S_n} \hat{\boldsymbol{\nu}}(\boldsymbol{x}) \cdot \nabla \, \Psi_j(\boldsymbol{x})|_+ \, \mathrm{dS}_{\boldsymbol{x}} = 0 \\ \Psi_j(\boldsymbol{x}) \to -E_0 x_j + \mathcal{O}(|\boldsymbol{x}|^{-2}) \text{ as } |\boldsymbol{x}| \to \infty \end{cases}$$

With similar arguments as above, we find that the eigenvalues of the high-contrast polarizability dyadic also scale with the volume. For the relation with the capacitance concept, we refer to Ref. 15.

References

[1] M. Abramowitz and I. A. Stegun, editors. *Handbook of Mathematical Functions.* Applied Mathematics Series No. 55. National Bureau of Standards, Washington D.C., 1970.

[2] K. V. Beard and C. C. Chuang. A new model for the equilibrium shape of raindrops. *J. Atmos. Sci.*, **44**(11), 1509–1524, 1986.

[3] J. Björkberg and G. Kristensson. Electromagnetic scattering by a perfectly conducting elliptic disk. *Canad. J. Phys.*, **65**(7), 723–734, 1987.

[4] C. F. Bohren and D. R. Huffman. *Absorption and Scattering of Light by Small Particles.* John Wiley & Sons, New York, 1983.

[5] L. J. Chu. Physical limitations of omni-directional antennas. *Appl. Phys.*, **19**, 1163–1175, 1948.

[6] R. E. Collin. *Field Theory of Guided Waves.* IEEE Press, New York, second edition, 1991.

[7] R. M. Fano. Theoretical limitations on the broadband matching of arbitrary impedances. *Journal of the Franklin Institute*, **249**(1,2), 57–83 and 139–154, 1950.

[8] M. Gustafsson. On the non-uniqueness of the electromagnetic instantaneous response. *J. Phys. A: Math. Gen.*, **36**, 1743–1758, 2003.

[9] F. John. Extremum problems with inequalities as subsidiary conditions. In O. E. Friedrichs, K. O. Neugebauer and J. J. Stoker, editors, *Studies and Essays: Courant Anniversary Volume*, pages 187–204. Wiley-Interscience, New York, 1948.

[10] D. S. Jones. Low frequency electromagnetic radiation. *J. Inst. Maths. Applics.*, **23**(4), 421–447, 1979.

[11] D. S. Jones. Scattering by inhomogeneous dielectric particles. *Quart. J. Mech. Appl. Math.*, **38**, 135–155, 1985.

[12] R. C. Jones. A generalization of the dielectric ellipsoid problem. *Phys. Rev.*, **68**(3–4), 93–96, 1945.

[13] H. W. E. Jung. Über die kleinste Kugel, die eine räumliche Figur einschliesst. *J. reine angew. Math.*, **123**, 241–257, 1901.

[14] U. Kaatze. Microwave dielectric properties of water. In A. Kraszewski, editor, *Microwave Aquametry*, chapter 2, pages 37–53. IEEE Press, New York, 1996.

[15] R. E. Kleinman and T. B. A. Senior. Rayleigh scattering. In V. V. Varadan and V. K. Varadan, editors, *Low and high frequency asymptotics*, volume 2 of *Acoustic, Electromagnetic and Elastic Wave Scattering*, chapter 1, pages 1–70. Elsevier Science Publishers, Amsterdam, 1986.

[16] G. Kristensson and P. C. Waterman. The T-matrix for acoustic and electromagnetic scattering by circular disks. *J. Acoust. Soc. Am.*, **72**(5), 1612–1625, 1982.

[17] L. D. Landau, E. M. Lifshitz, and L. P. Pitaevskiĭ. *Electrodynamics of Continuous Media.* Pergamon, Oxford, second edition, 1984.

[18] G. Mie. Beiträge zur Optik trüber Medien, speziell kolloidaler Metallösungen. *Ann. Phys. Leipzig*, **25**, 377–445, 1908.

[19] M. I. Mishchenko and L. D. Travis. Capabilities and limitations of a current FORTRAN implementation of the T-matrix method for randomly oriented, rotationally symmetric scatterers. *J. Quant. Spectrosc. Radiat. Transfer*, **60**(3), 309–324, 1998.

[20] R. G. Newton. *Scattering Theory of Waves and Particles.* Dover Publications, New York, second edition, 2002.

[21] H. M. Nussenzveig. *Causality and dispersion relations.* Academic Press, London, 1972.

[22] H. M. Nussenzveig. *Diffraction Effects in Semiclassical Scattering.* Cambridge University Press, Cambridge, U.K., 1992.

[23] J. A. Osborn. Demagnetizing factors of the general ellipsoid. *Phys. Rev.*, **67**, 351–357, 1945.

[24] E. M. Purcell. On the absorption and emission of light by interstellar grains. *J. Astrophys.*, **158**, 433–440, 1969.

[25] A. Sihvola, P. Ylä-Oijala, S. Järvenpää, and J. Avelin. Polarizabilities of Platonic solids. *IEEE Trans. Antennas Propagat.*, **52**(9), 2226–2233, 2004.

[26] J. W. Strutt. On the light from the sky, its polarization and colour. *Phil. Mag.*, **41**, 107–120 and 274–279, April 1871. Also published in Lord Rayleigh, Scientific Papers, volume I, Cambridge University Press, Cambridge, 1899.

[27] J. R. Taylor. *Scattering theory: the quantum theory of nonrelativistic collisions.* Robert E. Krieger Publishing Company, Malabar, Florida, 1983.

[28] E. C. Titchmarsh. *Introduction to the Theory of Fourier Integrals.* Oxford University Press, Oxford, second edition, 1948.

[29] H. Van de Hulst. *Light Scattering by Small Particles.* John Wiley & Sons, Inc., New York, 1957.

[30] A. D. Yaghjian. Electric dyadic Green's functions in the source region. *Proc. IEEE*, **68**(2), 248–263, 1980.